Article

SERS/TERS Characterization of New Potential Therapeutics: The Influence of Positional Isomerism, Interface Type, Oxidation State of Copper, and Incubation Time on Adsorption on the Surface of Copper(I) and (II) Oxide Nanoparticles

Edyta Proniewicz* and Tomasz K. Olszewski

Cite This: *J. Med. Chem.* 2022, 65, 4387−4400

Read Online

ACCESS | Metrics & More | Article Recommendations | SI Supporting Information

ABSTRACT: The aim of this study was to investigate how the oxidation state of copper (Cu(I) vs Cu(II)), the nature of the interface (solid/aqueous vs solid/air), positional isomerism, and incubation time affect the functionalization of the surface of copper oxide nanostructures by [(butylamino)(pyridine)methyl]-phenylphosphinic acid (PyPA). For this purpose, 2-, 3-, and 4-isomers of PyPA and the nanostructures were synthesized. The nanostructure were characterized by UV-visible spectroscopy (UV−vis), scanning electron microscopy (SEM), Raman spectroscopy (RS), and X-ray diffraction (XRD) analysis, which proved the formation of spherical Cu_2O nanoparticles (Cu_2ONPs; 1500−600 nm) and leaf-like CuO nanostructures (CuONSs; 80−180/400−700 nm, width/length). PyPA isomers were deposited on the surface of NSs, and adsorption was investigated by surface-enhanced Raman scattering (SERS) and tip-enhanced Raman scattering (TERS). The changes of adsorption on the surface of copper oxide NSs caused by the above-mentioned factors were described and the enhancement factor on this substrate was calculated.
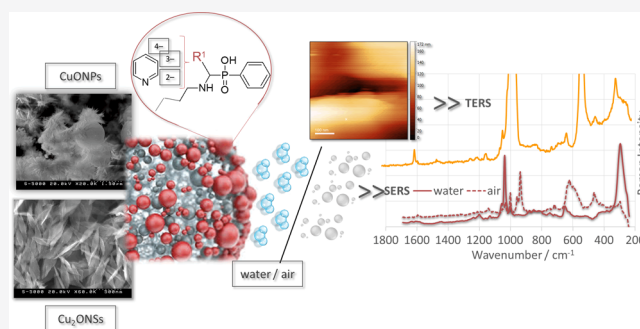
■ INTRODUCTION

The electronic and optical properties of metals depend on their surface structures. Nanostructures of metals (MNSs) are characterized by a high surface-to-volume ratio, a spectral shift in fluorescence emission, extremely low energy concentration efficiency, and the ability to localize optical fields at the nanoscale.[1−3] In addition, the interaction of the MNS surface with the surrounding medium is strong enough to prevail in density differences.[4] Magnetism, quantum confinement, enhanced toxic properties, lower melting temperature, and different light absorption compared to solid metals are also size-dependent properties of MNS.[4,5] Therefore, the methods for synthesizing MNSs have been improved to achieve a large active surface area[6] and nanoscale quantum confinement effects[7] in a medium free of surfactants to avoid any interference with the latter.[8,9] Among the various synthesized MNS, metal oxide nanostructures (MONSs) synthesized by anodic electrochemical dissolution of metals are particularly important due to their purity and unique electronic,[10] electrochemical,[11] catalytic,[12] and magnetic[13] properties.

Among metal oxides, copper oxides occupy an important place. Copper(I) oxide (Cu_2O) and copper(II) oxide (CuO), the most common initial corrosion product formed during the slow oxidation of metallic copper in contact with the atmosphere, play a special role because they are nontoxic,

cheap, and have unique optoelectronic properties, owing to which they have a broad range of technological and medical applications. Applications range from the production of electrodes, sensors, efficient photocatalysts driven by visible light,[14] solar energy conversion systems,[15] optoelectronics, lithium-ion batteries,[16] and superconductors[17] to cosmetics and textile components,[18] antiseptics, and bactericides used in daily life or to eliminate pathogens in the aquatic environment.[19]

CuO and Cu_2O are p-type semiconductors (E_g = 1.2−1.8 and 2.17 eV, respectively). Cu_2O belongs to the space group $Pn3m$ and crystallizes in a cubic structure with a lattice constant of a = 4.2696 Å, formed by a body-centered cubic (bcc) arrangement of oxygen atoms with metal atoms between two successive oxygen layers so that each oxygen atom is surrounded by a tetrahedron of copper atoms (a centered cubic (fcc) sublattice) and each metal atom has two coordinates forming linear CuO_2 units.[20] The length of the

Cu−O bonds in these units is 1.849 Å, which is smaller than in copper(II) oxide.[20] CuO belongs to the point symmetry group $2/m$ and crystallizes in a monoclinic structure,[21] in which the environment of the Cu(II) ions is strongly distorted by the strong Jahn−Teller effect. The lengths of the Cu−O bonds in square planar groups are larger than those in Cu_2O and are 1.88 and 1.96 Å.[22] The length of the two perpendiculars to the planar Cu−O bonds is much larger, which precludes octahedral coordination.

Due to the wide use of metal oxide nanoparticles, their release into the environment is inevitable. Some MONSs, such as copper oxide NSs, are susceptible to dissolution in environmental systems depending on the size of these nanoparticles, which is of particular concern in the plant rhizosphere.[22,23] This can lead to the simultaneous release of Cu ions from the surface, increasing the bioavailability of the surface layer and potentially causing negative responses in environmental systems (e.g., inhibition of plant growth) even at subtoxic concentrations of metal ions.[24] However, even less is known about the negative effects of copper oxide NPs on animal organisms. To this end, the influence of morphology (shape and size) and the concentration of copper oxide NPs on their antimicrobial activity have been studied.[25−27] For example, it was found that the antimicrobial activity (via the redox cycle between Cu(I) and Cu(II)[28]) of copper oxide NPs against pathogenic microorganisms depends on the oxidation state of copper (Cu(I) ions have a higher potency than Cu(II) ions), pH, size (<100 nm; a decrease in size leads to an increase in antimicrobial activity), and morphology.[29] Cu(II) ions in bacterial cells are thought to be reduced by sulfhydryl to Cu(I) ions, which are responsible for causing oxidative stress.[30] The smallest Cu_2ONPs showed the highest antimicrobial efficiency at intermediate concentrations compared to low (5 mg/mL) or high (200 mg/mL) concentrations.[22] Cu_2ONPs were also shown to induce apoptosis in HeLa and melanoma cells at lower concentrations than in normal human and mouse cell lines.[31] The selective cytotoxicity of copper oxide NPs in cancer cells was also described.[32] The endoplasmic reticulum stress-induced mechanism on copper oxide NPs has been found to play a role in the apoptosis of renal cancer cells.[25] Copper oxide NPs also generate reactive oxygen species (ROS) and damage mitochondrial membranes.[33] The photodynamic activity of copper oxide NPs, resulting from their ability to generate ROS when excited by light, can be used in photodynamic therapy for cancer treatment. However, the tumor-specific toxicity of copper oxide NPs to cancer cells is not yet clear. For example, the octahedral Cu_2O nanocrystals were shown to have higher photodynamic activity (greater killing capacity) compared to Cu_2ONPs with cubic and hexagonal shapes.[26] Moreover, the results show that the viability of cancer cells decreases correspondingly with increasing concentration of Cu_2ONPs after green laser irradiation.[26] Other results confirm the positive cytotoxic effect of copper oxide NSs on cancer cell lines by reducing angiogenesis and inducing apoptosis.[34,35] Other studies have developed nonenzymatic glucose sensors based on copper oxide NSs.[36,37] It has been also shown that the presence of copper accelerates the process of glucose oxidation and increases the stability of the sensor itself.

As mentioned above, the antibacterial and antifungal properties of copper oxide NSs and their potential use (e.g., for cancer imaging and therapy (shortening the relaxation time of the magnetic spin-lattice (T_1) and increasing the speed of

sound and ultrasound attenuation coefficient),[38,39] glucose sensors, etc.) were key factors choosing copper oxide NSs among other MONSs. Moreover, the positive cytotoxic effect of copper oxide NSs on cancer cell lines can possibly be enhanced by functionalizing their surface with compounds possessing antitumor activity. Derivatives of α-aminophosphinic acid possess antitumor properties.[40] Pyridine-containing phosphinic acids, which are used in medicine as new therapeutics for various diseases such as inflammation,[41] asthma,[42] diabetes,[43] malaria,[44] heart failure,[45] human immunodeficiency virus (HIV),[46] and cancer[47] are very stable and effective bifunctional metal complexes with hepatotoxic activity (especially Cu(II) ions).[48] They also show inhibitory activity toward bovine pancreatic chymotrypsin (12−25% inhibition).[49] For these reasons, they represent a very interesting target for modern organic synthesis, and further evaluation of their physicochemical properties could provide valuable information on their potential applications.[50,51] Also, the study of adsorption of the compounds, especially in the condensed phase where dissolved species accumulate at the interface between NSs and solution, is important for determining the adsorbate geometry with respect to the metal surface and the changes due to positional isomerism. Positional isomerism is known to affect the activity of compounds.[52] For example, an analysis of the substitution pattern in Food and Drug Administration (FDA)-approved drugs (95 drugs) showed that the pyridine ring was mostly 4-substituted (*para*), in 11 drugs in the 2- and 6-position (*ortho*), and 1 drug had a monosubstitution in the 2-position. In addition, 3 drugs had monosubstitution in the 3-position and 10 drugs had disubstitution in the 3- and 5-position (*meta*).[53]

Accurate characterization of adsorbate behavior is critical because differences in the intensity of surface-enhanced Raman scattering (SERS) bands can be misinterpreted. From a medical perspective, changes in the intensity of the SERS signals are interpreted quantitatively (in terms of the adsorbate concentration) without taking into account the fact that the intensity of SERS bands depends on the orientation of the adsorbate on the metal surface. Such a misinterpretation may lead to diminishing the biological/medical significance of surface-functionalized NSs.

For the abovementioned medical reasons, methods are sought to prepare pure, physiologically stable, and reagent-free (to exclude any environmental interference) copper oxide NSs with a specific and controlled morphology. The present work fits seamlessly into this search and describes a method for the preparation of copper oxide NSs that meets the abovementioned criteria and is based on the anodic electrochemical dissolution of copper. The copper oxide NSs were characterized spectroscopically, and then three isomers of α-aminophenylphosphinic acids of pyridine, including [(butylamino)(pyridin-2-yl)methyl]phenylphosphinic acid (2-PyPA), [(butylamino)(pyridin-3-yl)methyl]phenyl-phosphinic acid (3-PyPA), and [(butylamino)(pyridin-4-yl)methyl]-phenylphosphinic acid (4-PyPA) (see Figure 1 for the structures of these compounds), which have potential activity in cancer therapy, were synthesized and adsorbed onto their surfaces.

The resulting systems were characterized using the surface- and tip-enhanced Raman scattering techniques (SERS/TERS). Compared with other metal oxides, there are a limited number of reports on the use of unsupported copper oxide NSs as active substrates of SERS and for immobilization of small
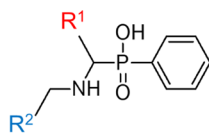
Compound abbreviation	R^1	R^2	UPAC Name
2-PyPA	2-Py	propane	[(butylamino)(pyridin-2-yl)methyl] phenylphosphonic acid
3-PyPA	3-Py	propane	[(butylamino)(pyridin-3-yl)methyl] phenylphosphonic acid
4-PyPA	4-Py	benzyl	[(benzylamino)(pyridin-4-yl)methyl] phenylphosphonic acid

Figure 1. Structure of the investigated α-aminophosphinic acid derivatives of pyridine.

molecules or molecules with high symmetry.[54−58] This is because aqueous copper oxide colloids are not as stable. This work shows for the first time how factors such as the oxidation state of the metal (Cu(I) vs Cu(II)), the contact interface (solid/water vs solid/air), incubation time, and positional isomerism [(butylamino)(pyridine)methyl]phenylphosphine (PyPA) affect adsorption. This work also shows that copper oxide NSs are not only effective substrates for SERS but can also act as potential drug carriers and sensitive (bio)sensors.

The studies at the solid/aqueous interface were carried out under physiological conditions, i.e., in the water environment. On the other hand, the studies at the solid/air interface were performed with a view to the practical application since not all measurements can be performed immediately (in the context of a large number of measurements or laboratory working hours) and/or nondrying of the sample is not always guaranteed (e.g., as a result of water evaporation due to heating of the sample (e.g., with laser radiation) or a long measurement period).

The shape and size of copper oxide NSs can be investigated by scanning/transmission electron microscopy (SEM/TEM), while X-ray diffraction (XRD) analysis provides information on the size and size distribution of crystalline domains. SERS allows the characterization of the adsorbate.[59−63] The only question is whether the SERS signal is from the adsorbate localized at the surface of the NSs or at "hot spots". Atomic force microscopy (AFM) combined with Raman spectrometry (TERS) answers this question. Thanks to nanometer resolution, TERS allows scanning the surface of the NSs and obtaining information about the geometry of the single molecule of the adsorbate.[64]

RESULTS AND DISCUSSION

Characterization of Cu₂ONPs. The SEM images (Figure 2A,B) show that the Cu₂ONPs are spherical and have a size of 1.5 μm to 600 nm. This size of the Cu₂ONPs is confirmed by the UV−vis spectrum, which shows two weak plasma resonances at 590 and 330 nm (Figure 2C, gray trace). The absorption at 590 nm is due to the band-gap transition of the CuO layer at the surface of the Cu₂O nanocrystals.[65] The absorption at 330 nm is due to the band-to-band transition in the nanocrystalline Cu₂O (O^{2-}:Cu^{1+} charge transfer (CT) band (O 2p → Cu 3d)).[66]

Cu₂ONPs show characteristic Raman bands at 630 cm^{-1} (T_{1u}), 486, 420, 219 (strongest E_u), 182, and 148 (T_{1u} symmetry) cm^{-1} (Figure 2D) consistent with data from the literature.[66,67] The 148 and 219 cm^{-1} bands are assigned to rotations of the Cu tetrahedron around its center. The 630 cm^{-1} spectral feature is due to out-of-plane vibrations of the Cu and O sublattice and is activated by defects (similar to the 148 cm^{-1} band).

The XRD spectrum of Cu₂ONPs (Figure 2E) shows diffraction peaks at 2θ values ([hkl], crystallographic plane): 77.61 [(311)], 73.69 [(200)], 61.54 [(211)], 42.44 [(200)], 36.52 [(111)], and 29.60 [(110)] (Pn3m; JCPDS No. 78-
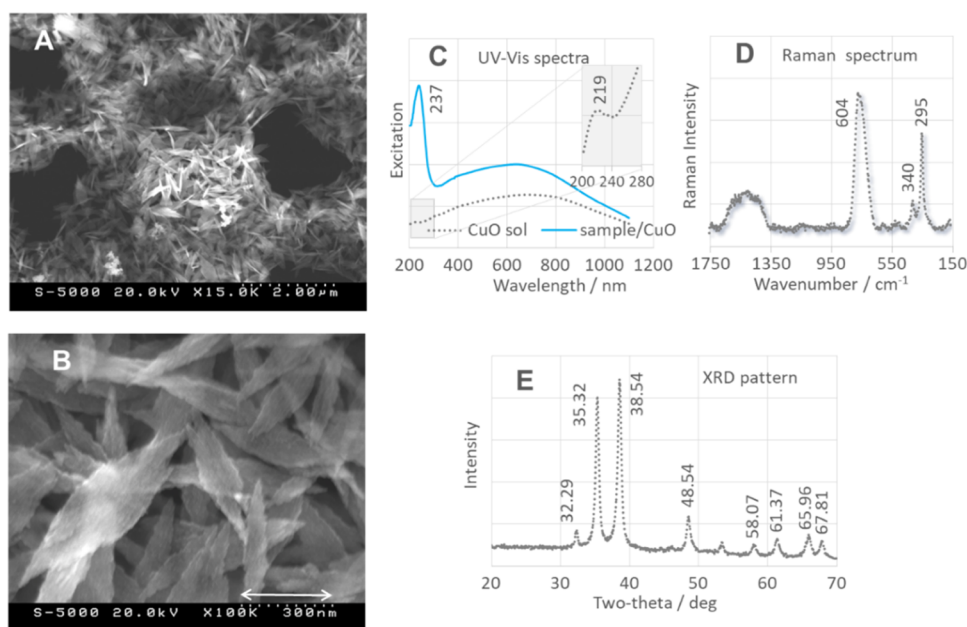

Figure 2. (A, B) SEM images of Cu₂ONPs (measurement conditions: (A)—20.0 kV, 3.0k×, scale 10.0 μm and (B)—20.0 kV, 20.0k×, scale 1.5 μm), (C) excitation spectra (UV−vis) of Cu₂ONPs (gray trace) and Cu₂ONPs/sample (green trace) used in this work, (D) Raman spectrum of Cu₂ONPs, and (E) XRD pattern of Cu₂ONPs.
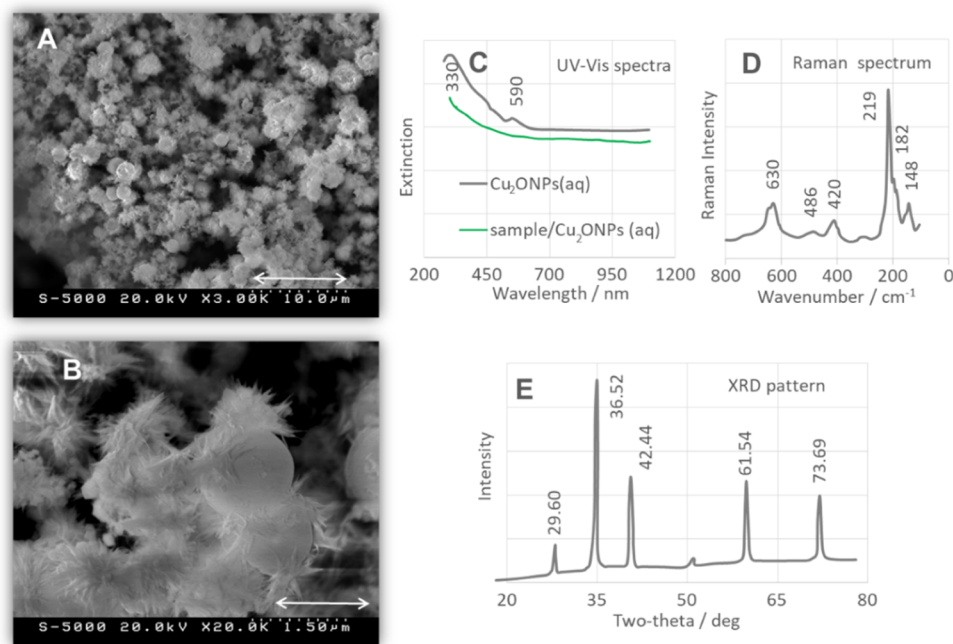
Figure 3. (A, B) SEM images of CuONSs (measurement conditions: (A)—20.0 kV, 3.0k×, scale 10.0 μm and (B)—20.0 kV, 20.0k×, scale 1.5 μm), (C) excitation spectra (UV−vis) of CuONSs (gray trace) and CuONSs/sample (green trace) used in this work, (D) Raman spectrum of CuONSs, and (E) XRD pattern of CuONSs.
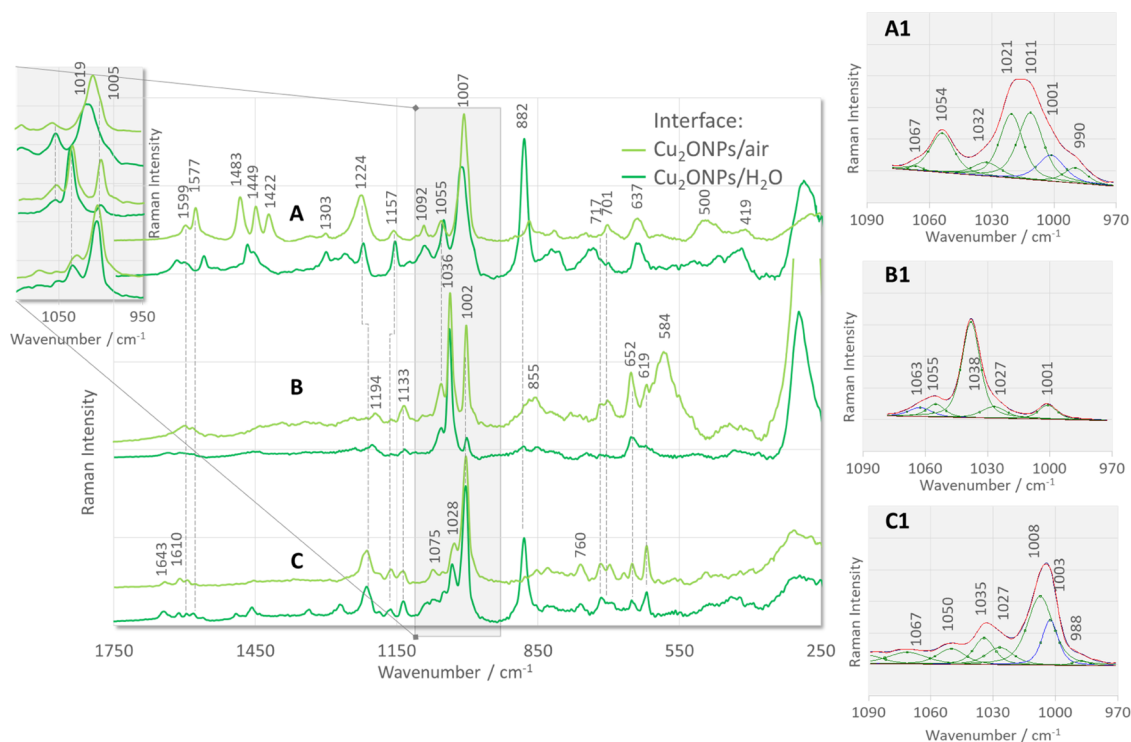

Figure 4. SERS spectra of the investigated 2- (A), 3- (B), and 4-isomers (C) of the pyridine α-aminophosphinic acid derivatives adsorbed on the Cu$_2$ONPs/water (green (bottom) lines) and Cu$_2$ONPs/air (aquamarine (upper) lines) interfaces (insets (A1)−(C1): fitting results of 2-, 3-, and 4-isomer spectra, respectively, in the spectral region of 970−1090 cm^{-1}).

2076), corresponding to a crystallographically pure, standard cubic cuprite structure.[68]

Characterization of CuONSs. The SEM images (Figure 3A,B) show that CuONSs have a leaf-like structure with average dimensions of 400−750 nm in length and 80−180 nm in width. The leaf-like structures consist of small self-aligned spherical particles (Figure 3B) and are confirmed by directional growth studies of CuO nanocrystals along the axis.[7,69] CuONSs form a skeleton resembling a honeycomb structure and consist a network of pores with a submicrometer diameter (2−3 μm) and thickness (1−1.5 μm thick) (Figure 3A).
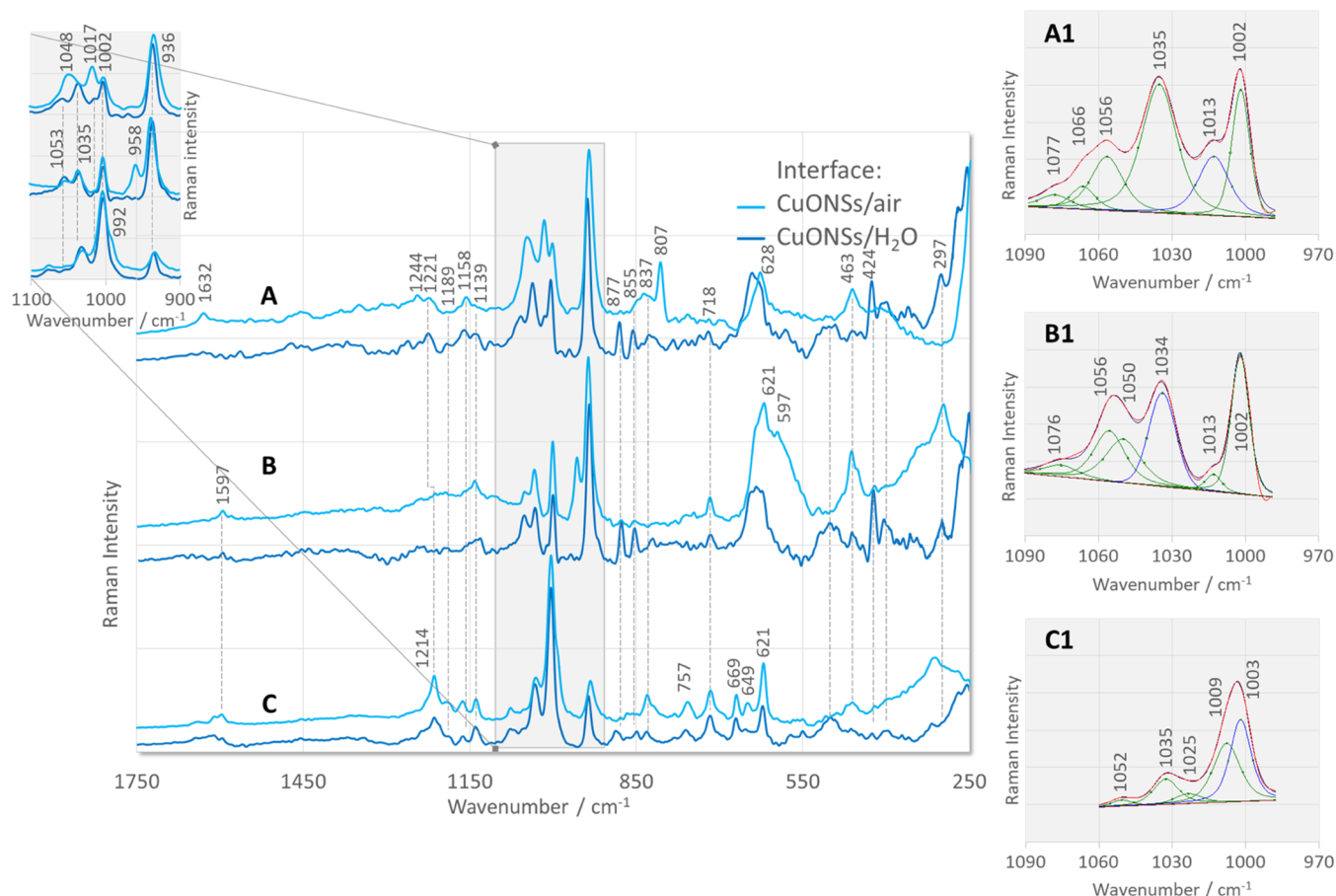
Figure 5. SERS spectra of the investigated 2- (A), 3- (B), and 4-isomers (C) of the pyridine α-aminophosphinic acid derivatives adsorbed on the CuONSs/water (navy (bottom) lines) and CuONSs/air (blue (upper) lines) interfaces (insets (A1)−(C1): fitting results of 2-, 3-, and 4-isomer spectra, respectively, in the spectral region of 970−1090 cm^{-1}).

In the UV−vis spectrum of the bare CuONSs (Figure 3C, a gray dashed line), a weak band is observed at 219 nm, which is attributed to direct electron transfer.[70−72] The spectrum of the sample/CuONSs (Figure 3C, a blue solid line), on the other hand, shows a broad absorption at 237 nm that is likely attributable to $\pi-\pi^*$ electronic transfer of the aromatic C=C groups of the molecule and/or CuONPs···adsorbate electrostatic interaction.[73]

The Raman spectrum of CuONSs (Figure 3D) shows three active Raman modes at 604 cm^{-1} (B_g), 340 (B_g), and 295 (A_g).[75] These bands indicate the pure monoclinic CuO structure.[7,74]

The XRD spectrum of CuONSs (Figure 3E) shows diffraction peaks at 2θ values: 67.81, 65.96, 65.96, 61.37, 58.07, 53.40, 48,54, 38.54, 35.32, and 32.29°, which are assigned to the [220], [31$\bar{1}$], [11$\bar{3}$], [202, 020], [20$\bar{2}$], [111]/ [200], [$\bar{1}$111]/[002], and [110] planes of the pure CuO nanophase with a monoclinic structure (JCPDS No. 48-1548).[76] The presence of highly crystalline CuONSs is confirmed by the significant intensity of the diffraction peaks.

Adsorption Monitored by SERS. Figure 4 shows the SERS spectra of the three isomers (2-, 3-, and 4-) of the derivative of pyridine α-aminophosphinic acid adsorbed at the Cu$_2$ONPs/H$_2$O (Figure 4, green lines) and Cu$_2$ONPs/air (Figure 4, aquamarine lines) interfaces. For comparison, the SERS spectra of these compounds adsorbed at the CuONSPs/ water (navy lines) and CuONSs/air (blue lines) interfaces are

shown in Figure 5. The proposed assignment of the bands to the normal modes describing the different vibrational motions in the molecule is summarized in Table 1. The given band assignment is not discussed in detail because an analysis of the potential energy distribution (PED) based on density functional theory (DFT/B3LYP6-311G(df,p)) has already been performed.[77] The band analysis presented also includes literature data on phenyl- and pyridine-substituted molecules.[78−81]

The pK_a values of the phosphinic acid group and the pyridine are below 6 and above 10, respectively. Therefore, the neutral form of these groups is expected to be present in the Cu$_2$ONPs sol at pH = 7, which is confirmed by the bands at 882 and 1138 cm^{-1} (see Table 1 for band assignment) in the spectra of the studied isomers (Figure 4, green lines).[82,83] The first of these bands is weakly enhanced in the Raman spectra of all of the isomers studied, while the second band has intermediate relative intensity (the intensity of the band is given with respect to the band with the highest intensity). The relative intensities of these bands differ in the SERS spectra. Briefly, in the 2-PyPA SERS spectrum at the Cu$_2$ONPs/H$_2$O interface (Figure 4A, green line), the 882 cm^{-1} band is the most intense band in the spectrum. In the 3-PyPA spectrum (Figure 4B, green line), this band is slightly enhanced, while in the 4-PyPA spectrum (Figure 4C, green line), it has about 60% of the intensity of the band in 2-PyPA. The second from the mentioned bands is weak in the spectra of all isomers (slightly

Table 1. Wavenumber of Selected Bands of the α-Aminophosphinic Acid Derivatives of Pyridine Adsorbed at the CuONSs/Water Interface[a]

bands assignment[a]	wavenumbers (cm^{-1})		
	2-PyPA	3-PyPA	4-PyPA
$\nu_{1Py} + \nu_{6bPy}$	1620	1636	1643
ν_{8aPy}	1603	1608	1610
ν_{8aPh}		1599	1597
ν_{8bPh}		1582	1580
	1563		1562
Ph	1471	1478	
Py	1458	1454	1457
$\nu_{19bPh}, \delta(CH_2/CH_3)$	1453	1442	
$\nu(P{=}O), \delta(C{-}C{-}H)$	1264	1239	1268
ν_{3Py}	1225	1201	1215
$\nu_{9aPy}, \nu_{7a}[C{-}C_{Ph}], \nu_{9aPh}$		1194	1188
$\nu(P{=}O), \delta(CH)$	1157	1160	1164
$\nu(P{-}OH)$	1138	1133	1135
ν_{18aPy}	1067[d]	1063[d]	1067[d]
ν_{18bPy}	1054[d]	1055[d]	1050[d]
ν_{12Py}	1032[d]	1038[d]	1035[d]
ν_{18aPh}	1021[d]	1027[d]	1027[d]
ν_{1Py}	1011[d]		1008[d]
ν_{12Ph}	1001[d]	1001[d]	1003[d]
	990[d]		988[d]
$\rho_b(POH)$	882	882	882
$\nu(P{-}O)$	854	855	855
	825		830
$\delta(Ph)$	761		760
$\nu_{4Py}, \nu(P{-}C_{Ph}), \rho_{as}(Ph), \nu(P{-}C), \delta(PCC_{Ph})$	738		716
$\nu_{6bPy}, \rho_{as}(Py) + \delta(C_{pyr}CP)$	645	652	651
ν_{6bPh}	623	619	621
Cu$\cdots$OH	459		463
Cu$\cdots$N	289		291

[a]Py, the pyridine ring; Ph, the phenyl ring; ν, stretching; δ, deformation; ρ_t, twisting; oop, out of plane; and as, antisymmetric vibrations; d, fitted bands.

enhanced only in 2-PyPA) and weaker than in the Raman spectra.

For strong band enhancement to occur at 882 cm^{-1} (in the case of 2-PyPA at Cu$_2$ONPs/H$_2$O), the lone pair of electrons on the oxygen atom (sp^3 hybridization) must be in direct contact with the surface of the nanoparticle, and therefore the sp^3 orbital occupied by the lone pair of electrons should be perpendicular to the substrate surface. This means that both the O–H bond and the O–P bond deviate from the normal to the surface of the substrate by an angle of 71°, i.e., the bonds are more or less parallel to the surface of the substrate (angle of 19°). Therefore, a very weak enhancement of the $\nu(P{-}O)$ mode can be expected for this isomer, which is observed. The decrease in the intensity of the 882 cm^{-1} band and a weak intensity of the 1135 cm^{-1} band for 4-PyPA compared to 2-PyPA could indicate a deviation of the sp^3 oxygen orbital with a lone pair of electrons with respect to the normal surface so that the angle between the O–P bond and the normal surface of the substrate decreases (i.e., the hydrogen atom approaches the surface of the substrate). In the case of the 3-PyPA isomer, the low intensity of the two bands discussed can be explained by the distance effect. That is, the phosphinic acid group is far from the surface of the substrate.

In the case of 2-PyPA at the Cu$_2$ONPs/H$_2$O interface, the intensity of the 882 cm^{-1} band depends on the incubation time of the isomer after mixing with the colloid (Figure 6), implying that the molecule on this interface reorients with time so that the O–H bond, which was originally practically parallel to the substrate surface, lifts to some extent relative to it. This can be seen in the following spectral changes. In the spectrum measured immediately after mixing ($t = 0$ s), the 882 cm^{-1} SERS signal is the second strongest band in the spectrum (after the 1012 cm^{-1} band) and has about 70% of the intensity of the 1012 cm^{-1} spectral feature. In the spectrum measured after 5 and 10 min of incubation, the 882 cm^{-1} band increases by about 30% each time. Further extension of the incubation time ($\geq$10 min) does not lead to any further changes in the enhancement of this band. For this isomer adsorbed on the surface of CuONSs (Figure 5A) and for the other isomers (3- and 4-) deposited on Cu$_2$ONPs (Figure 4B,C) and CuONSs (Figure 5B,C), the intensity of the 882 cm^{-1} band does not change with time. The orientation changes observed only for 2-PyPA are puzzling. Only for this isomer, the distance between the pyridine nitrogen atom and the phosphine oxygen atom, i.e., two atoms carrying a lone pair of electrons and therefore having a high affinity for a substrate surface, is the shortest, so that an intermolecular N$_{Py}\cdots$HO$_{phosphinic}$ hydrogen bond can be formed. The breaking of this bond due to the interaction with the Cu$_2$ONPs surface can be assumed as a probable explanation for the observed changes.

When the Cu$_2$ONPs/H$_2$O interface (Figure 4, green lines) is replaced by Cu$_2$ONPs/air (Figure 4, aquamarine lines), the intensity of the 1135 cm^{-1} band practically does not change and remains weak or very weak for all isomers studied, while the 882 cm^{-1} band is absent. This could be an indication of the deprotonation of the phosphinic acid group.

When the oxidation state of copper changes from Cu(I) to Cu(II), the type of interface (CuONSs/H$_2$O (Figure 5, navy lines) vs CuONSs/air (Figure 5, blue lines)) at which the molecules are adsorbed has a smaller effect on the behavior of the 877 cm^{-1} band; this spectral feature shows low intensity for all of the isomers at the CuONSs/H$_2$O interface ($I_{877\ 2\text{-PyPA}} \cong I_{877\ 3\text{-PyPA}} > I_{877\ 4\text{-PyPA}}$) and disappears at CuONSs/air. Thus, the isomerism of the substituent has practically no effect on the relative intensity of this band for molecules adsorbed on the surface of CuONSPs.

Time-dependent changes can also be seen in the other bands, of which those in the spectral range from 970 to 1080 cm^{-1} are of importance as they allow the determination of the change in the molecule–surface interaction. Within the abovementioned wavenumber range, seven bands can be identified (see Figure 7), which have been assigned to the vibrations of phenyl (ν_{12Ph} and ν_{18aPh}) and pyridine rings (ν_{1Py} (trigonal ring breathing involving C$_3$NC$_5$ atoms), ν_{12Py} (trigonal ring breathing involving C$_2$C$_4$C$_6$ atoms) and ν_{18bPy}).[84] Since we know that in the case of monosubstituted pyridine, the ν_{12} mode (e.g., the 3-isomer) or the ν_1 mode (e.g., the 2- and 4-isomers) becomes more dominant in the Raman spectra, and the ν_1 mode is not enhanced for the 3-isomer;[85] as can be seen in the SERS spectrum in Figure 4B (the fitting results for the isomer 3-), the following assignments of the abovementioned modes to bands can be made: 1002, 1020, 1010, 1034, and 1053 cm^{-1}.

In the 2-PyPA SERS spectrum at Cu$_2$ONPs/H$_2$O for $t = 0$ min. (Figure 6A), the ν_{12} mode of the phenyl ring (ν_{12Ph}) is weak, which may indicate that the phenyl ring is parallel to the
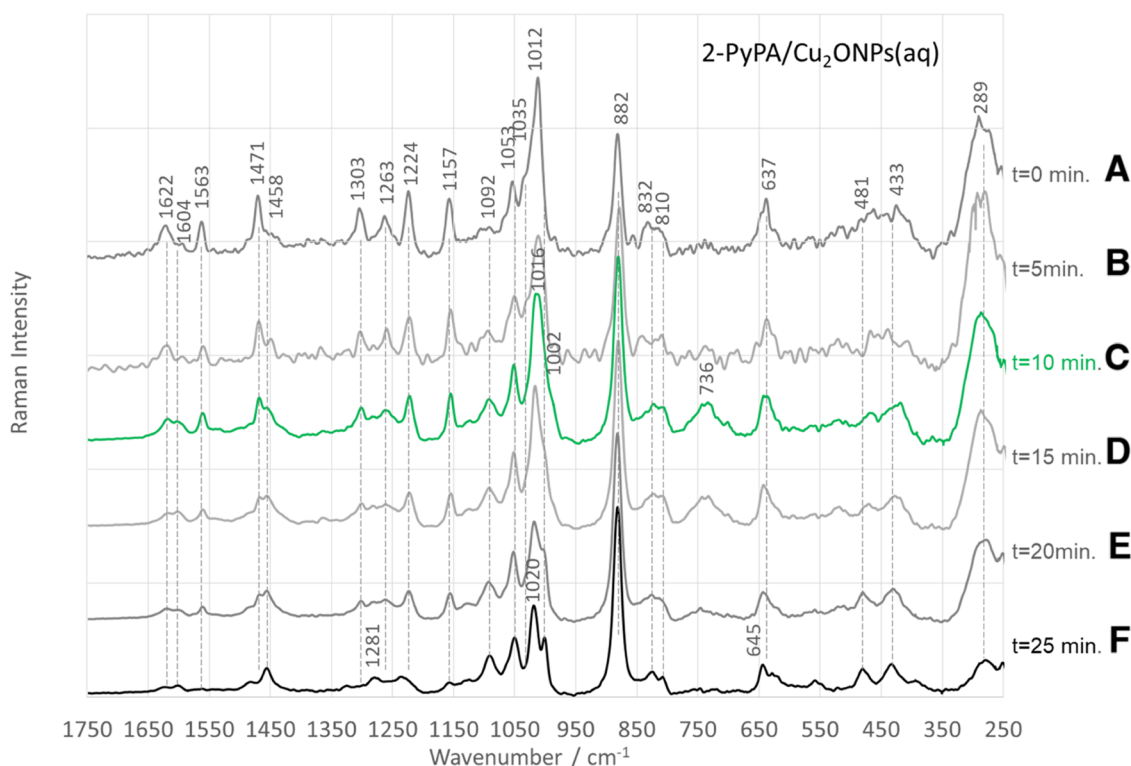
Figure 6. Time-dependent SERS spectra of the 2-PyPA isomer of the pyridine α-aminophosphinic acid derivative adsorbed on the Cu_2ONPs/H_2O interface (measured immediately after adsorption (t = 0 min) (A), t = 5 min (B), t = 10 min (C), t = 15 min (D), t = 20 min (E), and t = 25 min (F)).

Figure 7. Fitting results of the time-dependent SERS spectra of the 2-PyPA isomer of the pyridine α-aminophosphinic acid derivative adsorbed on the Cu_2ONPs/H_2O interface (measured immediately after adsorption (t = 0 min) (A), t = 5 min (B), t = 10 min (C), t = 15 min (D), t = 20 min (E), and t = 25 min (F)).
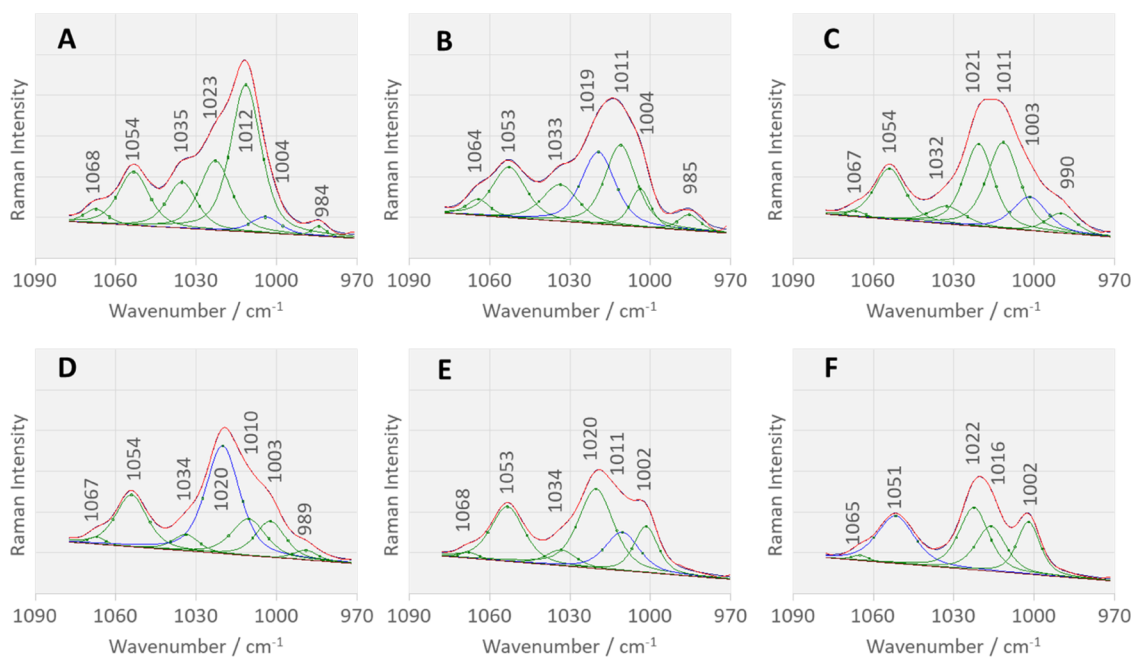
surface of the substrate compared to its high intensity in the Raman spectrum. This is confirmed by both the shift in its wavenumber ($\Delta\nu$ = +5 cm^{-1}) and the broadening of its bandwidth (Δ_{FWHM} = +6 cm^{-1}) compared to those in the Raman spectrum. The intensity of this band increases with increasing incubation time each time, up to an intensity

corresponding to three times its initial intensity (t = 25 min, Figure 6F). Thus, it can be assumed that the phenyl ring increases relative to the Cu_2ONPs/H_2O interface.

The increase in ν_{12Ph} intensity with increasing incubation time is accompanied by a change in the intensity of the SERS signals at 1012 and 1035 cm^{-1}. The 1012 cm^{-1} band is the

strongest in the SERS spectrum at $t = 0$ min (Figure 6A). In the SERS spectra at $t = 5$ and 10 min (Figure 6B,C), it has comparable intensity but loses 40% of intensity compared to the SERS spectrum at $t = 0$ min. In the spectra for a longer incubation time, i.e., $t = 15$ and 20 min (Figure 6D,E), it again loses about 50% of intensity. For a time $t = 25$ min (Figure 6F), it increases by about 15%. Jagodzinski and colleagues divided the spectra of pyridine adsorbed on various metal surfaces into two groups on the basis of the behavior of the bands at 1036, 1008, and 654 cm^{-1}.[84] In the spectra of the first group (end-on absorption orientation of Py on Ag), the bands are enhanced at 650 and 1036 cm^{-1}, with the 1036 cm^{-1} band having at least 50% of the intensity of the band at 1008 cm^{-1}. In the spectra of the second group (edge-on adsorption geometry of Py on Cu), the band at 1036 cm^{-1} is weak (it has at most 25% of the intensity of the band at 1008 cm^{-1}), and the band at 650 cm^{-1} is absent. Moreover, in the spectra of the latter group, the SERS signals at 1213, 1597, and 1640 cm^{-1} are stronger than in the spectra of the "end-on" group. The authors found that the 654 cm^{-1} SERS signal (B$_1$ point symmetry group) disappears at the copper surface and the 633 cm^{-1} spectral feature (A$_1$) appears. These authors also found that pyridine achieves equilibrium between "end-on" and "edge-on" (α-pyridyl) orientations on other metal surfaces, resulting in intermediate spectra between the spectra on Ag and Cu surfaces. Based on the abovementioned studies, it can be assumed that both forms of pyridine are present at the Cu$_2$ONPs/H$_2$O interface and that the equilibrium between these two forms in the first minutes after adsorption is shifted toward the "edge-on" form (at $t = 0$ min, intensity ratio $I_{1012}/I_{1023} = 3.5$ and bands at 637, 1224, 1563, and 1622 cm^{-1} are stronger than at $t = 25$ min) and shifts toward the "end-on" form with increasing incubation time (at $t = 25$ min, intensity ratio $I_{1012}/I_{1023} = 2.1$ and the band at 645 cm^{-1} is stronger than at $t = 0$ min). The intense SERS signal at 289 cm^{-1} min, which is due to Cu–N vibrations, can confirm this statement. The enhancement of this mode is strong at $t = 0$ min and decreases when the 2-PyPA molecule rotates at the edge and the pyridine turns into α-pyridyl. Therefore, the differences between the SERS spectra of 2-PyPA at different incubation times are due to the degree of conversion of pyridine to α-pyridyl species.[86]

The change of the interface type from Cu$_2$ONPs/H$_2$O to Cu$_2$ONPs/air leads to some changes in the spectral profile of the pyridine bands in the SERS spectrum of 2-PyPA (Figure 4A). The most important changes include the enhancement of the medium-intensity bands at 1577, 1483, 1449, and 1422 cm^{-1}, the attenuation of the spectral features at 1157 and 1055 cm^{-1}, the shift of the wavenumber of ν_{8bPy} and ν_{1Py}, the disappearance of the 1622 cm^{-1} SERS signal, and the significant broadening of the band at 1224 cm^{-1}. These changes can be explained on the basis of the work of Uvdal et al.[86] These authors have shown that in the SERS spectrum of pyridine, when the ring is arranged vertically and tilted on edge relative to the substrate surface, the bands due to A$_1$ and B$_1$ symmetry are mainly enhanced, whereas when the ring is tilted frontally, the A$_1$ and B$_2$ symmetry modes are mainly enhanced. In the present case, the 1157 and 1055 cm^{-1} bands are due to the B$_2$ symmetry modes, while 1577, 1483, 1449, 1422, and 1212 cm^{-1} SERS signals are due to the B$_1$ symmetry modes. Thus, the attenuation of the B$_2$ modes and the enhancement of the B$_1$ modes indicate a perpendicular arrangement of the pyridine ring, which is in contact with the substrate surface through its C–N bond.

In the spectrum of 3-PyPA on Cu$_2$ONPs (Figure 4B), a shift in the wavenumber of the bands in the blue direction is observed between the Raman and SERS spectra. The ν_{12Py} and ν_{3Py} modes are shifted from 1027 and 1201 cm^{-1} in the Raman spectrum to 1038 and 1224 cm^{-1} in the SERS spectrum. Similarly, in the 4-PyPA spectrum (Figure 4C), the ν_{1Py} mode is shifted from 1004 cm^{-1} in the Raman spectrum to 1008 cm^{-1} in the SERS spectrum. Suh et al. have shown that for isomers of pyridine carboxylic acid, the wavenumber shift of the pyridine modes due to adsorption on the surface is relatively small when the interaction with the metal surface through the nitrogen atom is weak.[87] This can be explained by the fact that the surface geometry of the pyridine ring is slightly inclined to the surface. The large shift of 11 cm^{-1} observed for 3-PyPA at Cu$_2$ONPs/H$_2$O correlates with higher vibrational energy and is indicative of a strong coordination bond (pyridine ring perpendicular to the Cu$_2$ONPs/H$_2$O interface). On the other hand, the 4 cm^{-1} shift in the wavenumber for 4-PyPA indicates that the pyridine ring is tilted with respect to the substrate surface compared to fully planar geometry. In a planar geometry, where no coordination bonds are formed, shifts are less likely because the bond between the pyridine ring and the surface is also much weaker and mostly physical.

Comparison of the fitting results of the spectra of 3-PyPA and 4-PyPA at the Cu$_2$ONPs/H$_2$O interface (Figure 4B1,C1) with the corresponding Raman spectra shows that the phenyl ring adopts a nearly parallel orientation on this interface for 3-PyPA (the 1001 and 1027 cm^{-1} SERS signals are weak) and is tilted for 4-PyPA (the 1003 and 1027 cm^{-1} bands are medium strength). Interestingly, the 4-PyPA isomer contains two phenyl rings in its structure, but only the vibrations of one of these rings are observed. Considering the optimized structure of this molecule[77] and the fact that the ρ_b(POH) mode in the SERS spectrum of 4-PyPA is observed at the Cu$_2$ONPs/H$_2$O interface, it can be assumed that this ring is a phenyl ring in the phosphinic acid group.

In the case of the 3-PyPA isomer, the change in the contact interface (Cu$_2$ONPs/H$_2$O → Cu$_2$ONPs/air) (Figure 4) mainly leads to a realignment of the phenyl ring from a practically parallel to a practically vertical position with respect to the surface, as evidenced by a significant increase in the band intensity at 1002 cm^{-1} (the second strongest band in the spectrum). In the case of 4-PyPA, only a slight attenuation of the intensity of some bands of the aromatic ring vibrations is observed. On this basis, it can be assumed that both the phenyl ring and the pyridine ring do not reorient. The change in the oxidation state of copper also affects the spectral profile so that the most intense bands in the spectra are at 936 and 1002 cm^{-1}. The 936 cm^{-1} spectral feature is most pronounced in the SERS spectra of 2-PyPA and 3-PyPA. This band is accompanied by 463 and 267 cm^{-1} spectral features and increasing and broadening bands in the spectral region between 500 and 650 cm^{-1}. These observations can be explained by the assumption that the CuONS modes (604 and 295 cm^{-1} (Figure 4)) overlap with the bands originating from the 2- and 3-PyPA modes and that protons are bound to the CuONS surface, leading to SERS signals at 936 [ν(Cu–OH)] and 490–460 cm^{-1}.[88−90]

The fitting procedure in the spectral region of 980−1090 cm^{-1} of the SERS spectra of the three discussed isomers adsorbed on the surface of CuONSs (Figure 5A1−C1) proves that these isomers interact with this surface via the pyridine and phenyl rings. However, the arrangement of these rings
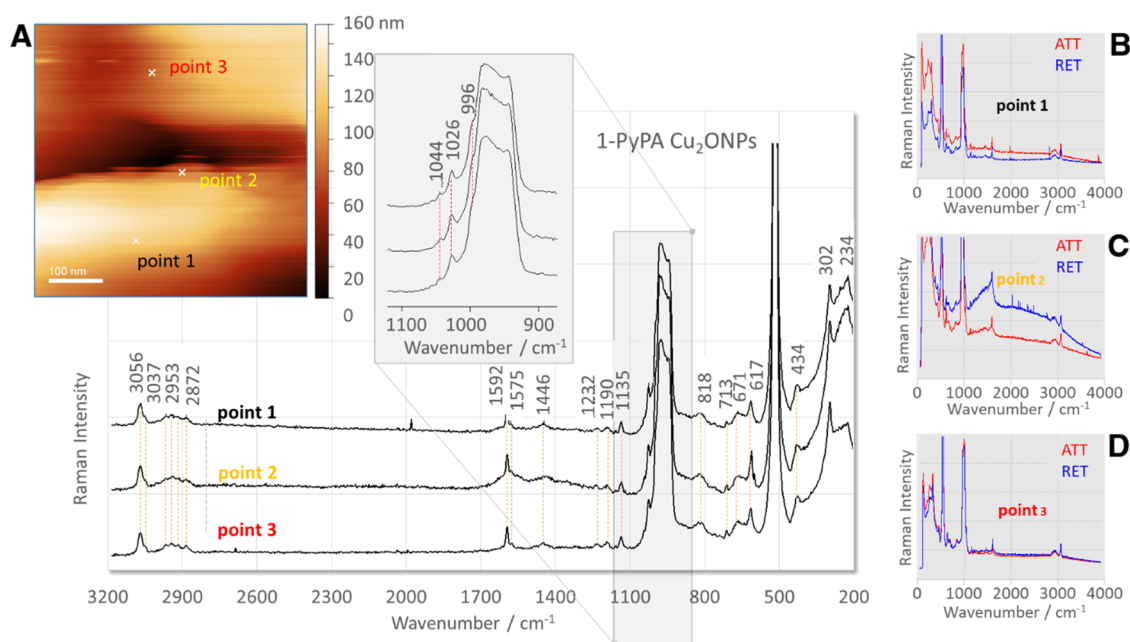
Figure 8. TERS spectra of the 2-PyPA isomer adsorbed on the Cu$_2$ONP surface (insets: (A) AFM image of Cu$_2$ONPs with marked measurement points and (B−D) spectra measured under the conditions of the approached (red traces) and retracted (blue traces) tip at measurement points 1, 2, and 3, respectively).

relative to the surface of CuONSs is altered compared to Cu$_2$ONPs. In the case of 2-PyPA at the CuONSs/H$_2$O interface, the intensity of the 1001 cm^{-1} band is higher than the intensity of the 1013 cm^{-1} SERS signal, while at the CuONSs/air interface, these intensities are reversed ($I_{1013} > I_{1002}$). In the SERS spectrum of 3-PyPA, the 1013 cm^{-1} band is weak (at CuONSs/H$_2$O) or absent (at CuONSs/air) (Figure 5A1,B1). For 4-PyPA, the ν_1 mode is hidden under the most pronounced 1003 cm^{-1} SERS signal and the wavenumber shifts upward when the molecule is immobilized at the CuONSs/H$_2$O interface or downward when immobilized at the CuONSs/air interface. From the abovementioned observations and the changes in the wavenumber of the SERS bands relative to the Raman bands ($\Delta\nu_{12Ph}$ = +3, +5, and +4 cm^{-1} for 2-, 3-, and 4-PyPA and $\Delta\nu_{1Py}$ = 21 cm^{-1} for 2-PyPA, $\Delta\nu_{12Py}$ = 8 cm^{-1} for 3-PyPA, and $\Delta\nu_{1Py}$ = 5 cm^{-1} for 4-PyPA), it can be concluded that the phenyl ring is tilted with respect to the CuONS surface for 2-PyPA and 3-PyPA and practically vertical for 4-PyPA and that its arrangement does not change practically when the interface changes from CuONSs/H$_2$O to CuONSs/air for the 3-PyPA and 4-PyPA isomers, while the phenyl ring is slightly more inclined for the 2-PyPA isomer. One could also speculate that the pyridine ring adopts an approximately vertical orientation with respect to the CuONSs/H$_2$O interface for 2-PyPA and a tilted one for the other isomers. In the case of the 4-PyPA isomer, the pyridine ring is less deviated from the surface normal and interacts with the surface via the pyrrole nitrogen (649 cm^{-1}, "end-on" orientation), while the broad band at 634 cm^{-1} for −PyPA might be related to the presence of pyridine in an equilibrium between "end-on" and "edge-on" orientation.

TERS Studies. Figure 8A shows an AFM image of the Cu$_2$ONP surface (scale bar 100 nm) with the three selected measuring points, where the TERS spectra of the 2-PyPA isomer were collected. Figure 8 shows the TERS spectra for the three abovementioned points obtained by subtracting the spectrum measured under the retracted tip conditions from the

spectrum acquired under the approached tip conditions (insets B−D). These TERS spectra show the bands characteristic of the weakly scattering 2-PyPA molecule, which are hardly detectable using normal Raman spectroscopy. Comparison of the TERS spectra at all measuring points shows good reproducibility of the measurements. The intensities of the bands in the TERS spectra recorded at the different measurement points differ only slightly. This is not surprising given that the size of Cu$_2$ONPs is very large compared to the size of the molecule in contact with the Cu$_2$ONPs. Thus, the molecule "fills" the surface of the Cu$_2$ONPs like a flat surface.

Comparison of the TERS spectra of 2-PyPA with the corresponding SERS spectrum at the Cu$_2$ONPs/air interface (Figure 4A, aquamarine line) shows the same series of bands (1597, 1575, 1446, 1232, 1190, 1135, 1044, 1026, 996, 818, 713, 671, 617, 424, and 302 cm^{-1}). However, the TERS signals are significantly enhanced and narrower compared to the corresponding SERS signals. Moreover, the TERS spectra are free from ambient interference and support the predicted mode of 2-PyPA adsorption mainly through the vertical α-pyridyl ring, and the phenyl ring and the deprotonated phosphine group are located near the surface of the substrate, which were submerged based on the SERS spectrum.

SERS Enhancement. The enhancement factor (EF) evaluates the effectiveness of the SERS substrate. The enhancement factor is often expressed as EF = (I_{SERS}/c_{SERS})/(I_{RS}/c_{RS}), where I_{SERS} and I_{RS} are the band intensities in the SERS and Raman spectra, respectively, and c_{SERS} and c_{RS} are the concentrations of the analyte used for SERS and Raman measurements, respectively.[91] For equal analyte concentrations, EF equas I_{SERS}/I_{RS}. The EF determined is up to 10^6 orders of magnitude for Ag and Au@SiO$_2$; 10^5 orders of magnitude for Au; 10^4 orders of magnitude for Cu and Ti; 10^3 orders of magnitude for ZnO, CuO, Cu$_2$O, TiO$_2$, and γ-Fe$_2$O$_3$; and 10^2 orders of magnitude for Zn and Fe.[92,93]

Using the SERS spectra, the mechanism of enhancement can be predicted for the analyte and the substrate. The mechanism

of enhancement can be predicted from the SERS spectra. The SERS spectrum of the molecule physically adsorbed on the metal surface (electromagnetic (EM) mechanism) is similar to the Raman spectrum of the free molecule.[94,95] The SERS spectrum of the molecule chemically adsorbed on the metal surface (charge transfer (CT) mechanism) changes drastically in the wavenumber and intensity compared to the corresponding Raman spectrum. This is because the adsorbate−molecule complex leads to drastic changes in the wavenumbers and intensities of the SERS bands of the adsorbate.[96] Otero et al. have shown that the CT mechanism causes the enormous SERS intensity of the ν_{8a} vibration. For this reason, in aromatic ring-containing adsorbates (e.g., pyridazine, pyridine, benzene, and their derivatives), it can be used as a marker band of enhancement by the CT mechanism.[96−98] Based on the abovementioned information and the fact that in the case of the SERS spectra of PyPA, no strong enhancement of the ν_{8a} mode is observed and the differences in wavenumber, intensity, and width of the SERS vs Raman bands of PyPA are small, it can be concluded that on the tested substrates, the EM mechanism is responsible for the signal enhancement.

CONCLUSIONS

In this work, Cu2O nanoparticles (Cu2ONPs) (spherical with an average size of 1500−600 nm; crystallized in a cubic cuprite structure) and the leaf-like nanostructures (CuONSs) (average size of 80−180 nm in width and 400−750 nm in length; crystallized in a monoclinic structure) were synthesized by anodic electrochemical dissolution of copper in ethanol or an aqueous solution with a LiCl electrolyte. The morphology, size, and structure of the copper oxide NSs were verified by SEM, XRD, UV−vis, attenuated total reflection-Fourier transform infrared spectroscopy (AT-FTIR), and Raman spectroscopy (RS). The mode of adsorption of the 2-, 3-, and 4-isomers of α-aminophosphinic acid derivatives of pyridine immobilized at Cu2ONPs/air and Cu2ONPs/aqueous solution and CuONSs/air and CuONSs/aqueous solution interfaces was observed at pH 7 at an excitation wavelength of 785.0 nm.

The investigations performed in this study showed that the oxidation state of the metal (Cu(I) vs Cu(II)), the nature of the contact interface (solid/water vs solid/air), and the positional isomerism of the adsorbate affect the geometry of the molecule on the copper oxide NS surface. In the case of the 2-isomer, the incubation time also affects the adsorption of this molecule at the Cu2ONPs/H2O interfaces, which can be explained by the breaking of the intermolecular $N_{Py}\cdots HO_{phosphinic}$ hydrogen bond under the influence of adsorption. For molecules adsorbed on the Cu2ONPs surface, many more changes are observed under the influence of the interface type (from Cu2ONPs/H2O to Cu2ONPs/air) than on the CuONS surface. That is, for 2-PyPA and 3-PyPA, the change of the contact interface causes not only changes in the orientation of the aromatic rings but also deprotonation of the phosphinic acid group.

The TERS spectra of 2-PyPA immobilized on Cu2ONPs recorded from different points on the surface show a high degree of similarity. This is because the molecule "fills" the Cu2ONP surface like a flat surface. In addition, the TERS measurements avoided interference from the surrounding environment, which obscures the SERS spectrum, thanks to the nanometer spatial resolution.

These studies have demonstrated the usefulness of Cu2ONPs and CuONSs as effective sensors for the studied

compounds with anticancer activity. Thus, the process of catalytic destruction of tumor cells could be enhanced by the introduction of copper oxide NSs with active compounds immobilized on their surface.

EXPERIMENTAL SECTION

Synthesis of Phenylphosphinic Acids. α-Aminophenylphosphinic acids of pyridine (Figure 1) were synthesized by the addition of silylated phosphoric acid esters to suitable pyridinimines.[99] The detailed synthetic procedure and NMR characterization of these compounds have been published previously.[100] All of the pyridine α-aminophenylphosphinic acids used in this study are present as racemic mixtures. The purity and chemical structures of the studied compounds were confirmed by ^{1}H, ^{13}C, and ^{31}P NMR spectra recorded on a JEOL 400yh instrument (400 MHz for ^{1}H NMR, 162 MHz for ^{31}P NMR, and 100 MHz for ^{13}C NMR) and processed with software Delta 5.0.5.

Synthesis of Copper Oxide Nanoparticles. Copper(I) oxide (cuprous oxide, Cu2ONPs) and copper(II) oxide (cupric oxide, CuONSs) nanoparticles were prepared by chronoamperometry (at room temperature and at a constant electrode potential of 0.8 V for 4 h).[101] A 0.1 M aqueous solution of lithium chloride (LiCl; from Sigma-Aldrich) was freshly prepared and used for CuONS synthesis, while an ethanolic LiCl solution with 10% water was freshly prepared and used for the synthesis of Cu2ONPs. The electrochemical treatment was carried out under an inert atmosphere by slowly bubbling the solution with argon gas in a conventional three-electrode cell with a platinum wire as a counter electrode and an Ag/AgCl (1 M KCl) electrode as a reference electrode (the potential is indicated against this electrode). A copper rod served as a working electrode. Before electrochemical treatment, metallic copper (99.99% Cu) was polished with sandpaper to reduce the grain size and then purified in anhydrous ethanol (99.8%; from Sigma-Aldrich). The precipitated product was in the form of orange Cu2ONPs and brown CuONSs.

Ultraviolet−Visible (UV−Vis) Spectroscopy Measurements. UV−vis spectra of an aqueous copper oxide NSs sol and a sample/copper oxide NSs system measured after 180 min of mixing were recorded using a Lambda 25 UV−vis spectrometer.

Scanning Electron Microscopy (SEM) Measurements. The SEM images of an aqueous copper oxide NSs sol were acquired using an SEM instrument, model S-5000 (Hitachi Ltd., Japan) at 20 kV.

X-ray Powder Diffraction (XRD) Measurements. Powder X-ray diffraction (XRD) spectra were measured using a Rigaku UltimaIV X-ray diffractometer (Rigaku Co., Japan) with Cu K_{α} ($\lambda = 1.542$ Å) radiation at 40 kV and 40 mA in the range 20−80° (2θ) with a step of 0.02.

Raman and Surface-Enhanced Raman Scattering (SERS) Measurements. Aqueous solutions of the studied compounds were prepared by dissolving each compound in deionized water (18 MΩ/cm; sample concentration 10^{-4} mol/dm^3; pH = 7). A total of 10 μL of the sample solution was mixed with 20 μL of the aqueous sol solution. Then, 20 μL of the sample/sol mixture was applied to a glass plate and the SERS spectra were recorded (no measurements were made for the dried droplet). The spectra were recorded three times at three different locations on each surface.

The Raman and SERS spectra were recorded using a HoloSpec f/1.8i spectrograph (Kaiser Optical Systems Inc.) equipped with a liquid-nitrogen-cooled CCD detector (Princeton Instruments). The 785.0 nm line of a NIR diode laser (Invictus) was used as an excitation source. The laser power at the sample position was set to ~15 mW. The typical exposure time for each SERS measurement was 40 s with four accumulations. The spectral resolution was set to 4 cm^{-1}. The SERS spectra of a given adsorbate on a given substrate were almost identical, except for small differences (up to 5%) in some band intensities. No spectral changes that could be associated with decomposition of the sample were observed during these measurements.

The spectra obtained were almost identical (very well reproducible) except for small differences (up to ~5%) in some band

intensities. No spectral changes that could be associated with sample decomposition or desorption processes were observed in these measurements.

Tip-Enhanced Raman Spectroscopy (TERS) Measurements. Aqueous sample solutions were prepared by dissolving the peptide in deionized water (18 MΩ/cm). The concentration of the sample was adjusted to 10^{-4} mol/dm^3 before mixing with the colloidally suspended Cu$_2$ONPs. Overall, 10 μL of the sample solution was mixed with 20 μL of Cu$_2$ONPs. The mixture was kept for 15 min before SERS measurement. For TERS measurements, the mixture was placed on a glass plate after 15 min of incubation and dried in a vacuum dryer at 37 °C for 30 min.

TERS measurements were performed in a top-illumination top-collection setup using a 514 nm DPSS laser (Cobalt Fandago 25), a 90× objective (NA = 0.71), and a liquid-nitrogen-cooled CCD detector (Princeton Instrument). The tips used for the measurements were electrochemically etched bulk silver tips (Unisoku Co. Ltd.) with an apex radius of ∼50 nm, located 45° from the sample plane. The tips were attached to a 32 kHz tuning fork and were controlled by a noncontact AFM with shear force. The same tips were used for both AFM and TERS. For each measured point, spectra were first recorded under conditions where the tip approached the sample (the distance between the tip and the sample was less than 2 nm), and then under conditions where the tip retraced. Subtraction between the two conditions yielded a spectrum with the signal due to near-field enhancement (without the far-field signal from outside the tip). The typical exposure time for each SERS measurement was 240 s with 3 accumulations and a 0.10 mW laser power.

Spectral Analysis. Spectral analysis was performed using a GRAMS/AI program (Galactic Industries Co., Salem, NH).

Multiple nonseparated bands were fitted using a GRAMS/AI program (Galactic Industries Co., Salem, NH). A 50/50% Lorentzian/Gaussian band shape was assumed and fixed for all bands.

ASSOCIATED CONTENT

Supporting Information

The Supporting Information is available free of charge at https://pubs.acs.org/doi/10.1021/acs.jmedchem.2c00031.

> General process for the preparation of PyPA; ^{31}P, ^{1}H, and ^{13}C NMR spectra (in D$_2$O) of compounds: 2-PyPA, 3-Py-PA, and 4-PyPA (PDF)
> Molecular formula strings (CSV)

AUTHOR INFORMATION

Corresponding Author

Edyta Proniewicz − *Faculty of Foundry Engineering, AGH University of Science and Technology, 30-059 Kraków, Poland; Department of Chemistry, School of Science and Technology, Kwansei Gakuin University, Sanda, Hyogo 669-137, Japan;* orcid.org/0000-0002-1872-2779; Email: proniewi@agh.edu.pl

Author

Tomasz K. Olszewski − *Faculty of Chemistry, Wroclaw University of Science and Technology, 50-370 Wroclaw, Poland*

Complete contact information is available at: https://pubs.acs.org/10.1021/acs.jmedchem.2c00031

Author Contributions

E.P. contributed to fundraising for research, research concept and design, synthesis of copper oxide nanostructures, spectroscopic measurements, data analysis, drawing figures and original manuscript writing, discussion with reviewers, and final version of manuscript and T.K.O. contributed to the synthesis of α-aminophosphinic acid derivatives of pyridine. All authors have given approval to the final version of the manuscript.

Notes

The authors declare no competing financial interest.

ABBREVIATIONS USED

Cu$_2$ONPs, copper(I) oxide nanoparticles; CuONSs, copper-(II) oxide nanostructures; PyPA, analogues of α-amino-phenylphosphinic acid of pyridine; SEM, scanning electron microscopy; SERS, surface-enhanced Raman scattering; TERS, tip-enhanced Raman scattering; UV−vis, ultraviolet−visible spectroscopy; XRD, X-ray diffraction analysis

REFERENCES

(1) Hewageegana, P. Theory of Electronic and Optical Properties of Nanostructures. Ph.D. Thesis, Georgia State University: Georgia, 2008.

(2) Tantra, R. *Nanomaterials Characterization: An Introduction*; John Wiley & Sons: Hoboken, New Jersey, 2016.

(3) Koole, R.; Groeneveld, E.; Vanmaekelbergh, D.; Meijerink, A.; de Mello Donegá, C. In *Nanoparticles*; de Mello Donegá, C., Ed.; Springer: Berlin, Heidelberg, 2014; Chapter 2.

(4) Visakh, P. M.; Martinez Morales, M. J. *Nanomaterials and Nanocomposites*; Viley-VCH: Weinheim, Germany, 2016.

(5) Gao, F.; Gu, Z. In *Handbook of Nanomaterials*; Aliofkhazraei, M., Ed.; Springer: Switzerland, 2016; pp 661−690.

(6) Besner, S.; Kabashin, A.; Winnik, F.; Meunier, M. Ultrafast laser based "green" synthesis of non-toxic nanoparticles in aqueous solutions. *Appl. Phys. A: Mater. Sci. Process* **2008**, *93*, 955−959.

(7) Bello, A.; Dodoo-Arhin, D.; Makgopa, K.; Fabiane, M.; Manyala, M. Surfactant Assisted Synthesis of Copper Oxide (CuO) Leaf-like Nanostructures for Electrochemical Applications. *Am. J. Mater. Sci.* **2014**, *4*, 64−73.

(8) Fan, M.; Brolo, A. G. Self-assembled Au nanoparticles as substrates for surface-enhanced vibrational spectroscopy: optimization and electrochemical stability. *Chem. Phys. Chem.* **2008**, *9*, 1899−1907.

(9) Wang, G.; Xiao, L.; Huang, B.; Ren, Z.; Tang, X.; Zhuang, L.; Lu, J. AuCu intermetallic nanoparticles: surfactant-free synthesis and novel electrochemistry. *J. Mater. Chem.* **2012**, *22*, 15769−15774.

(10) Kumar, A.; Buttry, D. A. Size-Dependent Anodic Dissolution of Water-Soluble Palladium Nanoparticles. *J. Phys. Chem. C* **2013**, *117*, 26783−26789.

(11) Karim, W. O. Anodic Dissolution of Metals in Ionic Liquids. Ph.D. Thesis, University of Leicester: Leicester, England, 2016.

(12) Gawande, M. B.; Goswami, A.; Felpin, F.-X.; Asefa, T.; Huang, X.; Silva, R.; Zou, X.; Zboril, R.; Varma, R. S. Cu and Cu-Based Nanoparticles: Synthesis and Applications in Catalysis. *Chem. Rev.* **2016**, *116*, 3722−3811.

(13) Stankic, S.; Suman, S.; Haque, F.; Vidic, J. Pure and multi metal oxide nanoparticles: synthesis, antibacterial and cytotoxic properties. *J. Nanobiotechnol.* **2016**, *14*, No. 73.

(14) Xu, C.; Wang, X.; Yang, L.; Wu, Y. Fabrication of a graphene−cuprous oxide composite. *J. Solid State Chem.* **2009**, *182*, 2486−2490.

(15) Siddiqui, H.; Parra, M. R.; Pandey, P.; Qureshi, M. S.; Haque, F. Z. Utility of copper oxide nanoparticles (CuO-NPs) as efficient electron donor material in bulk-heterojunction solar cells with enhanced power conversion efficiency. *J. Sci.: Adv. Mater. Devices* **2020**, *5*, 104−110.

(16) Waser, O.; Hess, M.; Güntner, A.; Novák, P.; Pratsinis, S. E. Size controlled CuO nanoparticles for Li-ion batteries. *J. Power Sources* **2013**, *241*, 415−422.

(17) Li, W. M.; Zhao, J. F.; Cao, L. P.; Hu, Z.; Huang, Q. Z.; Wang, X. C.; Yu, R. Z.; Long, Y. W.; Wu, H.; Lin, H. J.; Chen, C. T.; Gong, Z. Z.; Guguchia, Z.; Kim, J. S.; Stewart, G. R.; Uemura, Y. J.; Uchida, S.; Jin, C. Q. The Unconventional Copper Oxide Superconductor with Conventional Constitution. *J. Supercond. Novel Magn.* **2020**, *33*, 81−85.

(18) Román, L. E.; Gomez, E. D.; Solís, J. L.; Gómez, M. M. Antibacterial Cotton Fabric Functionalized with Copper Oxide Nanoparticles. *Molecules* **2020**, *25*, No. 5802.

(19) Guerrero Correa, M.; Martínez, F. B.; Vidal, C. P.; Streitt, C.; Escrig, J.; Lopez de Dicastillo, C. Antimicrobial metal-based nanoparticles: a review on their synthesis, types and antimicrobial action. *Beilstein J. Nanotechnol.* **2020**, *11*, 1450−1469.

(20) Korzhavyi, P. A.; Johansson, B. *Literature Review on the Properties of Cuprous Oxide Cu2O and the Process of Copper Oxidation*. Technical Report TR-11-08; Svensk Kärnbränslehantering AB, Swedish Nuclear Fuel and Waste Management Co., 2011.

(21) Su, D.; Xie, X.; Dou, S.; Wang, G. CuO single crystal with exposed {001} facets - A highly efficient material for gas sensing and Li-ion battery applications. *Sci. Rep.* **2015**, *4*, No. 5753.

(22) Xiong, L.; Yu, H.; Nie, C.; Xiao, Y.; Zeng, Q.; Wang, G.; Wang, B.; Lv, H.; Li, Q.; Chen, S. Size-controlled synthesis of Cu2O nanoparticles: size effect on antibacterial activity and application as a photocatalyst for highly efficient H2O2 evolution. *RSC Adv.* **2017**, *7*, 51822−51830.

(23) McManus, P. Rhizosphere Interactions between Copper Oxide Nanoparticles and Wheat Root Exudate in a Sand Matrix; Influences on Bioavailability and Uptake. Graduate Thesis, Utah State University, 2016.

(24) Wang, Y.; Zi, X.-Y.; Su, J.; Zhang, H.-X.; Zhang, X.-R.; Zhu, H. Y.; Li, J.; Yin, M.; Yang, F.; Hu, Y. Cuprous oxide nanoparticles selectively induce apoptosis of tumor cells. *Int. J. Nanomed.* **2012**, *7*, 2641−2652.

(25) Yang, Q.; Wang, Y. C.; Yang, Q.; Gao, Y.; Duan, X.; Fu, Q.; Chu, Ch.; Pan, X.; Cui, X.; Sun, Y. Cuprous oxide nanoparticles trigger ER stress-induced apoptosis by regulating copper trafficking and overcoming resistance to sunitinib therapy in renal cancer. *Biomaterials* **2017**, *146*, 72−85.

(26) Bhaisare, M. L.; Khan, M. S.; Pandey, S.; Gedda, G.; Wu, H.-F. Shape-oriented photodynamic therapy of cuprous oxide (Cu2O) nanocrystals for cancer treatment. *RSC Adv.* **2017**, *7*, 23607−23614.

(27) Taherzadeh-Soureshjani, P.; Chehelgerdi, M. Algae-meditated route to cuprous oxide (Cu2O) nanoparticle: differential expression profile of MALAT1 and GAS5 LncRNAs and cytotoxic effect in human breast cancer. *Cancer Nanotechnol.* **2020**, *11*, No. 11.

(28) Bezza, F. A.; Tichapondwa, S. M.; Chirwa, E. M. N. Fabrication of monodispersed copper oxide nanoparticles with potential application as antimicrobial agents. *Sci. Rep.* **2020**, *10*, No. 16680.

(29) Meghana, S.; Kabra, P.; Chakrabortyb, S.; Padmavathy, N. Understanding the pathway of antibacterial activity of copper oxide nanoparticles. *RSC Adv.* **2015**, *5*, 12293−12299.

(30) Wang, W.; Ren, J.; Sun, S.; Zhang, L.; Wang, L.; Chang, J. Crystallography Facet-Dependent Antibacterial Activity, The Case of Cu2O. *Ind. Eng. Chem. Res.* **2011**, *50*, 10366−10369.

(31) Henson, T. E.; Navratilova, J.; Tennant, A. H.; Bradham, K. D.; Rogers, K. R.; Hughes, M. F. *In vitro* intestinal toxicity of copper oxide nanoparticles in rat and human cell models. *Nanotoxicology* **2019**, *13*, 795−811.

(32) Shafagh, M.; Rahmani, F.; Delirezh, N. CuO nanoparticles induce cytotoxicity and apoptosis in human K562 cancer cell line via mitochondrial pathway, through reactive oxygen species and P53. *Iran. J. Basic Med. Sci.* **2015**, *18*, 993−1000.

(33) Sarfraz, S.; Javed, A.; Mughal, S. S.; Bashir, M.; Rehman, A.; Parveen, S.; Khushi, A.; Khan, M. K. Copper Oxide Nanoparticles: Reactive Oxygen Species Generation and Biomedical Applications. *Int. J. Comput. Theor. Chem.* **2020**, *8*, 40−46.

(34) Azizi, M.; Ghourchian, H.; Yazdian, F.; Dashtestani, F.; Zeinabad, H. A. Cytotoxic effect of albumin coated copper nanoparticle on human breast cancer cells of MDA-MB 231. *PLoS One* **2017**, *12*, No. e0188639.

(35) Benguigui, M.; Weitz, I. S.; Timaner, M.; Kan, T.; Shechter, D.; Perlman, O.; Sivan, S.; Raviv, Z.; Azhari, H.; Shaked, Y. Copper oxide nanoparticles inhibit pancreatic tumor growth primarily by targeting tumor initiating cells. *Sci. Rep.* **2019**, *9*, No. 12613.

(36) Maaoui, H.; Teodoresu, F.; Wang, Q.; Pan, G. H.; Addad, A.; Chtourou, R.; Szunerits, S.; Boukherroub, R. Non-Enzymatic Glucose Sensing Using Carbon Quantum Dots Decorated with Copper Oxide Nanoparticles. *Sensors* **2016**, *16*, No. 1720.

(37) Wang, W.; Zhang, L.; Tong, S.; Li, X.; Song, W. Three-dimensional network films of electrospun copper oxide nanofibers for glucose determination. *Biosens. Bioelectron.* **2009**, *25*, 708−714.

(38) Zhou, M.; Tian, M.; Li, C. Copper-Based Nanomaterials for Cancer Imaging and Therapy. *Bioconjugate Chem.* **2016**, *27*, 1188−1199.

(39) Perlman, O.; Weitz, I. S.; Azhari, H. Copper oxide nanoparticles as contrast agents for MRI and ultrasound dual-modality imaging. *Phys. Med. Biol.* **2015**, *60*, 5767−5783.

(40) Hudson, H. R.; Lee, R. J. A Brief Review of the Anticancer Activity of α-Aminophosphonic Acid Derivatives and a Report on the in Vitro Activity of Some Dialkyl α-aryl- (or Heteroaryl)-α-(Diphenylmethylamino)Methanephosphonates. *Phosphorus, Sulfur Silicon Relat. Elem.* **2014**, *189*, 1149−1155.

(41) Lassaux, P.; Hamel, M.; Gulea, M.; Delbruck, H.; Mercuri, P. S.; Horsfall, L.; Dehareng, D.; Kupper, M.; Frere, J.-M.; Hoffmann, K.; Galleni, M.; Bebrone, C. Mercaptophosphonate Compounds as Broad-Spectrum Inhibitors of the Metallo-β-lactamases. *J. Med. Chem.* **2010**, *53*, 4862−4876.

(42) Maryanoff, B. E. Inhibitors of Serine Proteases as Potential Therapeutic Agents: The Road from Thrombin to Tryptase to Cathepsin G. *J. Med. Chem.* **2004**, *47*, 769−787.

(43) Combs, A. P. Recent Advances in the Discovery of Competitive Protein Tyrosine Phosphatase 1B Inhibitors for the Treatment of Diabetes, Obesity, and Cancer. *J. Med. Chem.* **2010**, *53*, 2333−2344.

(44) Haemers, T.; Wiesner, J.; Van Poecke, S.; Goeman, J.; Henschker, D.; Beck, E.; Jomaa, H.; Van, S. Calenbergh, Synthesis of α-substituted fosmidomycin analogues as highly potent Plasmodium falciparum growth inhibitors. *Bioorg. Med. Chem. Lett.* **2006**, *16*, 1888−1891.

(45) Kumar, T. S.; Zhou, S.-Y.; Joshi, B. V.; Balasubramanian, R.; Yang, T.; Liang, B. T.; Jacobson, K. A. Structure−Activity Relationship of (N)-Methanocarba Phosphonate Analogues of 5′-AMP as Cardioprotective Agents Acting Through a Cardiac P2X Receptor. *J. Med. Chem.* **2010**, *53*, 2562−2576.

(46) Robbins, B. L.; Srinivas, R. V.; Kim, C.; Bischofberger, N.; Fridland, A. Anti-human immunodeficiency virus activity and cellular metabolism of a potential prodrug of the acyclic nucleoside phosphonate 9-R-(2-phosphonomethoxypropyl)adenine (PMPA), Bis(isopropyloxymethylcarbonyl)PMPA. *Antimicrob. Agents Chemother.* **1998**, *42*, 612−617.

(47) Kang, S.-U.; Shi, Z.-D.; Worthy, K. M.; Bindu, L. K.; Dharmawardana, P. G.; Choyke, S. J.; Bottaro, D. P.; Fisher, R. J.; Burke, T. R., Jr. Examination of Phosphoryl-Mimicking Functionalities within a Macrocyclic Grb2 SH2 Domain-Binding Platform. *J. Med. Chem.* **2005**, *48*, 3945−3948.

(48) Videla, L. A.; Fernandez, V.; Tapia, G.; Varela, P. Oxidative stress-mediated hepatotoxicity of iron and copper: Role of Kupffer cells. *BioMetals* **2003**, *16*, 103−111.

(49) Olszewski, T. Original Syntheses of New Biomolecules; from Imidazole and Thiazole Derivatives of α-Aminophosphonic Acids and γ-Amino-α-, β-Dihydroxy Carboxylic Acids Derivatives to Disaccharide Mimics. Ph.D. Thesis, Wroclaw University of Technology: Poland, 2006.

(50) Żymańczyk-Duda, E.; Dunal, N.; Brzezińska-Rodak, M.; Osiewała, A.; Olszewski, T. K.; Klimek-Ochab, M.; Serafin-Lewańczuk, M. First biological conversion of chiral heterophospho-

nate derivative − Scaling and paths of conversion discussion. *Bioorg. Chem.* **2019**, *93*, No. 102751.

(51) Wolińska, E.; Hałdys, K.; Góra, J.; Olszewski, T. K.; Boduszek, B.; Latajka, R. Phosphonic and Phosphinic Acid Derivatives as Novel Tyrosinase Inhibitors: Kinetic Studies and Molecular Docking. *Chem. Biodiversity* **2019**, *16*, No. e1900167.

(52) Wang, Y.; Hu, H.; Jing, S.; Wang, Y.; Sun, Z.; Zhao, B.; Zhao, C.; Lombardi, J. R. Enhanced Raman scattering as a probe for 4-mercaptopyridine surface-modified copper oxide nanocrystals. *Anal. Sci.* **2007**, *23*, 787−791.

(53) Ling, Y.; Hao, Z.-Y.; Liang, D.; Zhang, C.-L.; Liu, Y.-F.; Wang, Y. The Expanding Role of Pyridine and Dihydropyridine Scaffolds in Drug Design. *Drug Des., Dev. Ther.* **2021**, *15*, 4289−4338.

(54) Lee, J.-Y.; Han, J.; Lee, J.; Ji, S.; Yeo, J. S. Hierarchical Nanoflowers on Nanograss Structure for a Non-wettable Surface and a SERS Substrate. *Nanoscale Res. Lett.* **2015**, *10*, No. 505.

(55) Proniewicz, E.; Tąta, A.; Starowicz, M.; Szkudlarek, A.; Pacek, J.; Molenda, M.; Kuśtrowski, P. Ions-free electrochemically synthetized in aqueous media flake-like CuO nanostructures as SERS reproducible substrates for the detection of neurotransmitters. *Spectrochim. Acta, Part A* **2019**, *215*, 24−33.

(56) Balčytis, A.; Ryu, M.; Seniutinas, G.; Juodkazyt, J.; Cowie, B. C. C.; Stoddart, P. R.; Zamengo, M.; Morikawac, J.; Juodkazis, S. Black-CuO: surface-enhanced Raman scattering and infrared properties. *Nanoscale* **2015**, *7*, 18299−18304.

(57) Guo, H.; Ding, L.; Mo, Y. Adsorption of 4-mercaptopyridine onto laser-ablated gold, silver and copper oxide films: A comparative surface-enhanced Raman scattering investigation. *J. Mol. Struct.* **2011**, *991*, 103−107.

(58) Krajczewski, J.; Ambroziak, R.; Kudelski, A. Substrates for Surface-Enhanced Raman Scattering Formed on Nanostructured Non-Metallic Materials: Preparation and Characterization. *Nanomaterials* **2021**, *11*, No. 75.

(59) Wang, Y.; Yan, B.; Chen, L. SERS Tags: Novel Optical Nanoprobes for Bioanalysis,. *Chem. Rev.* **2013**, *113*, 1391−1428.

(60) Lin, D.; Qin, T.; Wang, Y.; Sun, X.; Chen, L. Graphene Oxide Wrapped SERS Tags: Multifunctional Platforms toward Optical Labeling, Photothermal Ablation of Bacteria, and the Monitoring of Killing Effect. *ACS Appl. Mater. Sci.* **2014**, *6*, 1320−1329.

(61) Payne, T. D.; Klawa, S. J.; Jian, T.; Kim, S. H.; Papanikolas, M. J.; Freeman, R.; Schultz, Z. D. Catching COVID: Engineering Peptide-Modified Surface-Enhanced Raman Spectroscopy Sensors for SARS-CoV-2. *ACS Sens.* **2021**, *6*, 3436−3444.

(62) Wang, R.; Li, J.; Rigor, J.; Large, N.; El-Khoury, P. Z.; Rogachev, A. Y.; Kurouski, D. Direct Experimental Evidence of Hot Carrier-Driven Chemical Processes in Tip-Enhanced Raman Spectroscopy (TERS). *J. Phys. Chem. C* **2020**, *124*, 2238−2244.

(63) El-Khoury, P. Z.; Schultz, Z. D. From SERS to TERS and Beyond: Molecules as Probes of Nanoscopic Optical Fields. *J. Phys. Chem. C* **2020**, *124*, 27267−27275.

(64) Jiang, N.; Kurouski, D.; Pozzi, E. A.; Chiang, N.; Hersam, M. C.; Van Duyne, R. P. Tip-enhanced Raman spectroscopy: From concepts to practical applications. *Chem. Phys. Lett.* **2016**, *659*, 16−24.

(65) Proniewicz, E.; Starowicz, M.; Ozaki, Y. Determination of the Influence of Various Factors on the Character of Surface Functionalization of Copper(I) and Copper(II) Oxide Nanosensors with Phenylboronic Acid Derivatives. *Langmuir* **2022**, *38*, 557−568.

(66) Pestryakov, A. N.; Petranovskii, V. P.; Kryazhov, A.; Ozhereliev, O.; Pfander, N.; Knop-Gericke, A. Study of copper nanoparticles formation on supports of different nature by UV−visible diffuse reflectance spectroscopy. *Chem. Phys. Lett.* **2004**, *385*, 173−176.

(67) Anu, A.; Khadara, M. A. Grain size tuning of nanostructured Cu₂O films through vapour phase supersaturation control and their characterization for practical applications. *AIP Adv.* **2015**, *5*, No. 097176.

(68) Yin, M.; Wu, C.-K.; Lou, Y.; Burda, C.; Koberstein, J. T.; Zhu, Y.; O'Brien, S. Copper Oxide Nanocrystals. *J. Am. Chem. Soc.* **2005**, *127*, 9506−9511.

(69) Zhao, B.; Liu, P.; Zhuang, H.; Jiao, Z.; Fang, T.; Xu, W.; Lu, B.; Jiang, Y. Hierarchical self-assembly of microscale leaf-like CuO on graphene sheets for high-performance electrochemical capacitors. *J. Mater. Chem. A* **2013**, *1*, 367−373.

(70) Kozak, D. S.; Sergiienko, R. A.; Shibata, E.; Iizuka, A.; Nakamura, T. Non-electrolytic synthesis of copper oxide/carbon nanocomposite by surface plasma in super-dehydrated ethanol. *Sci. Rep.* **2016**, *6*, No. 21178.

(71) Dhineshbabu, N. R.; Rajendran, V.; Nithyavath, N.; Vetumperumal, R. Study of structural and optical properties of cupric oxide nanoparticles. *Appl. Nanosci.* **2016**, *6*, 933−939.

(72) Tahir, D.; Tougaard, S. Electronic and optical properties of Cu, CuO and Cu₂O studied by electron spectroscopy. *J. Phys.: Condens. Matter* **2012**, *24*, No. 175002.

(73) El-Trass, A.; ElShamy, H.; El-Mehasseb, I.; El-Kemary, M. CuO nanoparticles: Synthesis, characterization, optical properties and interaction with amino acids. *Appl. Surf. Sci.* **2012**, *258*, 2997−3001.

(74) Hagemann, H.; Bill, H.; Sadowski, W.; Walker, E.; Francois, M. Raman spectra of single crystal CuO. *Solid State Commun.* **1990**, *73*, 447−451.

(75) Tran, T. H.; Nguyen, V. T. Phase transition of Cu2O to CuO nanocrystals by selective laser heatin. *Mater. Sci. Semicond. Process.* **2016**, *46*, 6−9.

(76) Zheng, S.; Hu, J. S.; Zhong, L. S.; Song, W. G.; Wan, L. J.; Guo, Y. G. Introducing Dual Functional CNT Networks into CuO Nanomicrospheres toward Superior Electrode Materials for Lithium-Ion Batteries. *Chem. Mater.* **2008**, *20*, 3617−3622.

(77) Piĝta, E.; Proniewicz, E.; Kudelski, A.; Olszewski, T. K.; Boduszek, B. Vibrational characterization of α-aminophosphinic acid derivatives of pyridine: DFT, Raman, and SERS spectroscopy studies. *Vib. Spectrosc.* **2016**, *83*, 115−125.

(78) Podstawka, E.; Kudelski, A.; Proniewicz, L. M. Adsorption mechanism of physiologically active L-phenylalanine phosphonodipeptide analogues: Comparison of colloidal silver and macroscopic silver substrates. *Surf. Sci.* **2007**, *601*, 4971−4983.

(79) López Tocón, I.; Woolley, M. S.; Otero, J. C.; Marcos, J. I. Vibrational spectrum of 3-methyl and 4-methylpyridine. *J. Mol. Struct.* **1998**, *470*, 241−246.

(80) Podstawka, E.; Kudelski, A.; Olszewski, T. K.; Boduszek, B. Surface-Enhanced Raman Scattering Studies on the Interaction of Phosphonate Derivativesof Imidazole, Thiazole, and Pyridine with a Silver Electrode in Aqueous Solution. *J. Phys. Chem. B* **2009**, *113*, 10035−10042.

(81) Proniewicz, E.; Pięta, E.; Zborowski, K.; Kudelski, A.; Boduszek, B.; Olszewski, T. K.; Kim, Y.; Proniewicz, L. M. Raman, surface-enhanced Raman, and density functional theory characterization of (diphenylphosphoryl)(pyridin-2-, -3-, and -4-yl)methanol. *J. Phys. Chem. A* **2014**, *118*, 5614−5625.

(82) Proniewicz, E.; Gralec, B.; Boduszek, B.; Olszewski, T. K. Aqueous platinum nanoparticles solution for the detection of pyridine derivatives of α-aminophosphinic acid. Influence of positional isomerism. *Appl. Surf. Sci.* **2017**, *425*, 941−947.

(83) Podstawka, E.; Drąg, M.; Oleksyszyn, J. Raman and surface-enhanced Raman studies of α-aminophosphinic inhibitors of metalloenzymes. *J. Raman Spectrosc.* **2009**, *40*, 1564−1571.

(84) Zuo, C.; Jagodzinski, P. W. Surface-Enhanced Raman Scattering of Pyridine Using Different Metals: Differences and Explanation Based on the Selective Formation of α-Pyridyl on Metal Surfaces. *J. Phys. Chem. B* **2005**, *109*, 1788−1793.

(85) Mühlig, A.; Cialla-May, D.; Popp, J. Fundamental SERS Investigation of Pyridine and Its Derivates as a Function of Functional Groups, Their Substitution Position, and Their Interaction with Silver Nanoparticles. *J. Phys. Chem. C* **2017**, *121*, 2323−2332.

(86) Andersson, M. P.; Uvdal, P. Transformation of Pyridine to α-Pyridyl on W(110) As Probed by Vibrational Spectroscopy: Experiments and Calculations. *J. Phys. Chem. B* **2001**, *105*, 9458−9462.

(87) Suh, J. S.; Kim, J. Three distinct geometries of surface-adsorbed carboxylate groups. *J. Raman Spectrosc.* **1998**, *29*, 143−148.

(88) Deng, Y.; Handoko, A. D.; Du, Y.; Xi, S.; Yeo, B. S. In Situ Raman Spectroscopy of Copper and Copper Oxide Surfaces during Electrochemical Oxygen Evolution Reaction: Identification of Cu^{III} Oxides as Catalytically Active Species. ACS Catal. **2016**, 6, 2473−2481.

(89) Pereira, D. C.; de Faria, D. L. A.; Constantino, V. R. L. Cu^{II} Hydroxy Salts: Characterization of Layered Compounds by Vibrational Spectroscopy. J. Braz. Chem. Soc. **2006**, 17, 1651−1657.

(90) Boehm, H. P. Acidic and basic properties of hydroxylated metal oxide surfaces. Discuss. Faraday Soc. **1971**, 52, 264−275.

(91) Le Ru, E. C.; Blackie, E.; Meyer, M.; Etchegoin, P. Surface Enhanced Raman Scattering Enhancement Factors: A Comprehensive Study. J. Phys. Chem. C **2007**, 111, 13794−13803.

(92) Proniewicz, E.; Tąta, A.; Wójcik, A.; Starowicz, M.; Pacek, J.; Molenda, M. SERS activity and spectroscopic properties of Zn and ZnO nanostructures obtained by electrochemical and green chemistry methods for applications in biology and medicine. Phys. Chem. Chem. Phys. **2020**, 22, 28100−28114.

(93) Proniewicz, E.; Tąta, A.; Szkudlarek, A.; Świder, J.; Molenda, M.; Starowicz, M.; Ozaki, Y. Electrochemically synthesized γ-Fe$_2$O$_3$ nanoparticles as peptide carriers and sensitive and reproducible SERS biosensors. Comparison of adsorption on γ-Fe$_2$O$_3$ versus Fe. Appl. Surf. Sci. **2019**, 495, No. 143578.

(94) Moskovits, M.; Suh, J. S. Surface geometry change in 2-naphthoic acid adsorbed on silver. J. Phys. Chem. A **1988**, 92, 6327−6329.

(95) Greaves, S. J.; Griffith, W. P. Vibrational spectra of catechol, catechol-d$_2$ and -d$_6$ and the catecholate monoanion. Spectrochim. Acta, Part A **1991**, 47, 133−140.

(96) Arenas, J. F.; Woolley, M. S.; López-Tocón, I.; Otero, J. C.; Marcos, J. I. Complete analysis of the surface-enhanced Raman scattering of pyrazine on the silver electrode on the basis of a resonant charge transfer mechanism involving three states. J. Phys. Chem. B **2000**, 112, 7669−7683.

(97) Arenas, J. F.; Soto, J.; López-Tocón, I.; Fernández, D. J.; Otero, J.; Marcos, J. I. The role of charge-transfer states of the metal-adsorbate complex in surface-enhanced Raman scattering. J. Phys. Chem. C **2002**, 116, 7207−7216.

(98) Castro, J. L.; López Ramírez, M. R.; López Tocón, I.; Otero, J. C. Vibrational study of the metal−adsorbate interaction of phenyl-acetic acid and α-phenylglycine on silver surfaces. J. Colloid Interface Sci. **2003**, 263, 357−363.

(99) Boduszek, B. Application of Bromotrimethylsilane and Trialkyl Phosphites for Convenient and Effective Synthesis of Amino-phoshonic Acids and Corresponding Monoalkyl and Dialkyl Esters. Pol. J. Chem. **2001**, 75, 663−672.

(100) Boduszek, B.; Olszewski, T.; Goldeman, W.; Konieczna, M. Aminophosphinic Acids in a Pyridine Series: Cleavage of Pyridine-2- and Pyridine-4-methyl(amino)phosphinic Acids in Acidic Solutions. Phosphorus, Sulfur Silicon Relat. Elem. **2006**, 181, 787−795.

(101) Starowicz, M. Electrochemical synthesis of copper oxide particles with controlled oxidation state, shape and size. Mater. Res. Express **2019**, 6, No. 0850a3.

NOTE ADDED AFTER ASAP PUBLICATION

This paper was originally published ASAP on March 1, 2022. A revised Supporting Information file was uploaded, and the paper was reposted on March 2, 2022.